J. Fluid Mech. (1981), *vol.* 111, *pp.* 87–106
Printed in Great Britain

A 'turbulent spot' in an axisymmetric free shear layer. Part 3. Azimuthal structure and initiation mechanism

By S. J. KLEIS, A. K. M. F. HUSSAIN, AND M. SOKOLOV†
Department of Mechanical Engineering, University of Houston, Texas 77004

(Received 30 June 1980 and in revised form 3 February 1981)

The details of a spark-induced 'spot' in an axisymmetric mixing layer of a 12·7 cm diameter (D) free air jet have been educed in different azimuthal planes and at three streamwise stations corresponding to x/D = 1·5, 3·0, 4·5. The measurement technique and the spot properties in the plane of the spark at the three stations were discussed in parts 1 and 2 (Sokolov *et al.* 1980 and Hussain, Kleis & Sokolov 1980, hereinafter referred to as I and II, respectively). The present part describes the azimuthal structure of the spot and its initiation mechanism.

It is shown that the distributions of phase-average longitudinal and lateral velocities, the intermittency and the coherent Reynolds stress within the spot are essentially the same in various azimuthal planes at each streamwise location. The spark induces a local boundary-layer spot on the nozzle wall and simultaneously triggers the instability of the free shear layer downstream from the lip. The boundary-layer spot persists initially in the free shear layer but decays downstream due to the lack of a sustaining mechanism. The mixing-layer spot – the result of a roll-up of a natural instability mode triggered in the free shear layer by the acoustic disturbance radiated from the spark – grows downstream and undergoes intense interactions, remaining essentially axisymmetric and travelling at about 60% of the core fluid velocity. Velocity signals in different azimuthal planes of the free shear layer show that the natural instability of the jet occurs axisymmetrically on an instantaneous basis even though the jet diameter is considerably larger than the instability wavelength. The natural instability is amplitude-modulated in a random manner; this modulation is also essentially axisymmetric.

The large-scale coherent structures produced by the intense localized spark are not only axisymmetric on the phase-average basis, but are also individually axisymmetric in the laminar instability region.

1. Background

In an attempt to study the dynamics of the large-scale coherent structure in the turbulent shear flow, a spark was fired in the boundary layer preceding the lip of an axisymmetric jet. The evolution in the free shear layer of the induced coherent structure, called a 'spot', was educed at three downstream stations (identified as stations 1, 2 and 3) corresponding to the x/D values of 1·5, 3·0 and 4·5, respectively. x is the downstream co-ordinate along the jet axis from the exit plane, and D is the

† Present address: School of Engineering, Tel-Aviv University, Israel.

jet diameter. Contours of the phase-average properties like longitudinal and transverse coherent and background velocity fluctuations, vorticity, intermittency, streamlines, pseudo-stream-function and coherent and background Reynolds stresses over the physical extent of the spot in the azimuthal plane passing through the middle of the localized spark were presented and the spot dynamics discussed in I and II. The evolution of the mixing-layer spot and the eduction of its features are much more complicated than those in the boundary-layer spot (Wygnanski, Sokolov & Friedman 1976; Zilberman, Wygnanski & Kaplan 1977; Cantwell, Coles & Dimotakis 1978).

Since the completion of the work reported in I and II, we became interested in the mechanism of formation of the spot as well as in the azimuthal dependence of its features. The present paper summarizes our findings on both of these aspects. The new data reveal surprising and interesting details of the spot-formation mechanism and the azimuthal characteristics of the spark-triggered spot.

2. Apparatus and procedure

This study has been carried out in the axisymmetric mixing layer of a 12·7 cm diameter air jet at the exit velocity U_e of 20 m s^{-1}. The exit centre-line longitudinal fluctuation intensity was 0·3 %. The jet discharges into a laboratory with controlled temperature, humidity and traffic, and the experiment was performed under remote control of a laboratory computer (HP2100S) so that the flow can be regarded to be free from ambient recirculation and turbulence as well as operator-induced disturbances (Kotsovinos 1976; Bradshaw 1977). Further details of the facility were given by Husain & Hussain (1979*a*).

The exit boundary layer was laminar with a shape factor value nearly equal to the Blasius profile value of 2·59. Initial mean and r.m.s. longitudinal fluctuation intensity profiles at different azimuthal planes indicated that the exit flow was axisymmetric. Since the virtual origin x_0 ($\simeq -0{\cdot}13D$) was very close to the exit, for convenience and following Bruun (1977), we have used $\eta \equiv (r-\frac{1}{2}D)/x$ as the transverse co-ordinate; r is the radius from the jet axis. For correspondence between η = constant lines with U/U_e = constant lines as well as some details of the basic flow state, see I.

Data were taken at different azimuthal planes identified by the azimuthal angle α. $\alpha = 0°$ represented the reference plane, i.e. plane passing through the middle point of the spark and the jet axis. For detailed data in the $\alpha = 0°$ plane, see I and II. In order to capture the azimuthal details of the spot, it was necessary to obtain data in different α planes. Because of symmetry about the azimuthal plane through the spark, data were needed only in a half-plane, i.e. over the range $0 \leqslant \alpha \leqslant 180°$. The extremely time-consuming data analysis process involved forced data acquisition to be limited to a few α angles. Thus, data were taken in planes corresponding to $\alpha = 0°$, 45°, 90°, 135° and 180°. Furthermore, data were taken only in a few limited radial positions, i.e. at the jet centre-line and along lines corresponding to $\eta = 0{\cdot}12$, 0·06, 0, and $-0{\cdot}06$. Thus, the transverse resolution of the data is lower than those presented for $\alpha = 0°$. Since $\alpha = 0°$ plane data were presented in I and II, this paper will present data in the planes for $\alpha = 45°$, 90°, 135° and 180° only.

For the longitudinal and lateral fluctuations $u(t)$, $v(t)$, data-acquisition and

analysis procedures were the same as those reported in I and II. That is, 200 successive realizations of $u(t)$, $v(t)$ and intermittency $I(t)$ signals capturing the spot signature were recorded digitally. Note that the structure-passage duration was about 4% of the period between successive sparks so that each spot is independent of the preceding and following ones. In order to enhance the spot features, these realizations were time-aligned with respect to each other through an iterative process of maximization of cross-correlation of each realization with the ensemble average. The alignment process was accelerated by low-pass filtering each signal at 500 Hz. Realizations requiring excessive time shifts for alignment were considered 'freak' and were discarded. For the details of the rejection ratio and histograms of time shifts at different radial and axial locations for $\alpha = 0°$, see I. Radial variations of the rejection ratio and histograms of time shifts at $\alpha = 45°$, 90°, 135° and 180° were essentially the same as for $\alpha = 0°$ (presented in I). Consequently, these profiles are not presented. The $v(t)$ and intermittency $I(t)$ signals were time-aligned such that the time shifts are the same as those required for the corresponding $u(t)$ traces.

For the instability study, $u(t)$ signals were obtained with eight single hot wires, seven of these in an azimuthal configuration mounted equi-spaced on a ring placed concentric with the jet axis. These wires were aligned azimuthally and adjusted to be located at $U/U_e = 0{\cdot}8$ at each x. The eighth hot wire was placed on the jet centreline. Linearized signals from these eight hot wires were recorded on analog tapes by an 8-channel tape-recorder (HP 3968A) which has a frequency response of 5 kHz and subsequently analysed. The jet nozzle and the probe arrangement are shown in figure 1.

3. Results and discussion

3.1. *Spot azimuthal structure*

The dynamics of the coherent structures and their convection velocity can be studied by plotting the pseudo-stream function derived from the phase-average longitudinal velocity distributions $u_p(T)$ (see II; Hussain & Zaman 1980). The values of the pseudo-stream function $\langle\psi\rangle \equiv \int_0^r r'(u_p - U_c)\,dr'$ were computed for each station at each α. These are the approximate instantaneous phase average streamlines viewed from a reference frame convected downstream with the velocity $U_c = 0{\cdot}66U_e$, which was found to be the average convection velocity of the structure (see II). Use of the Taylor hypothesis in deducing the spatial extent of the coherent structure from time traces was found to be least objectionable when drawn with respect to the structure convection velocity (Zaman & Hussain 1981).

The contours of $\langle\psi\rangle$ for $x/D = 1{\cdot}5$, $3{\cdot}0$ and $4{\cdot}5$ are shown in figures 2, 3, and 4, respectively. In each figure, cases (*a*), (*b*), (*c*) and (*d*) denote the azimuthal planes corresponding to $\alpha = 45°$, 90°, 135° and 180°, respectively.

The $\langle\psi\rangle$ contours bring out the approximate boundaries of the spot. Note that the structure centre at each station is essentially at the same location in different α planes. For example, the spot centre is at $T \simeq 21{\cdot}4$, 36 and 49 ms for $x/D = 1{\cdot}5$, $3{\cdot}0$ and $4{\cdot}5$, respectively. These locations agree with the data in the $\alpha = 0°$ plane (see II). However, the contour details, especially the η-location of the spot centre indicated by the $\langle\psi\rangle$ contours, show some differences. For $x/D = 1{\cdot}5$, the contours at $\alpha = 45°$

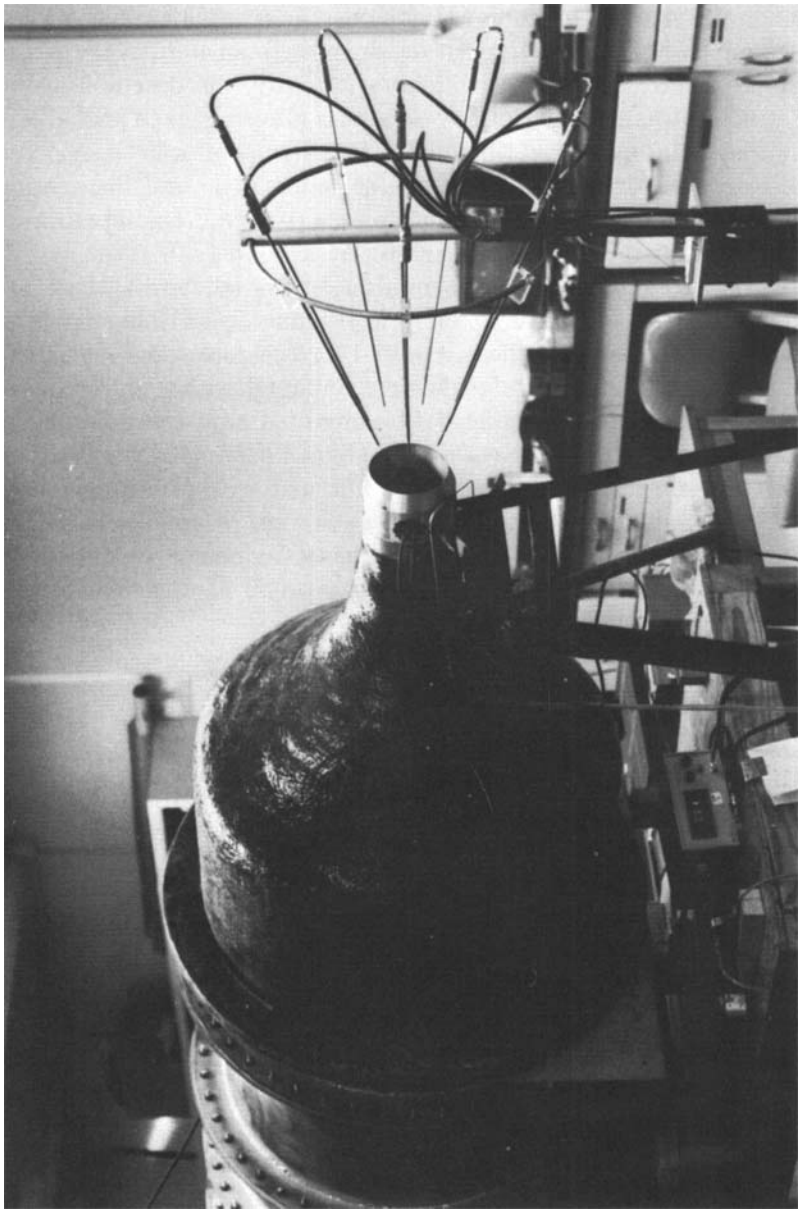

FIGURE 1. The probe arrangement for the instability study.

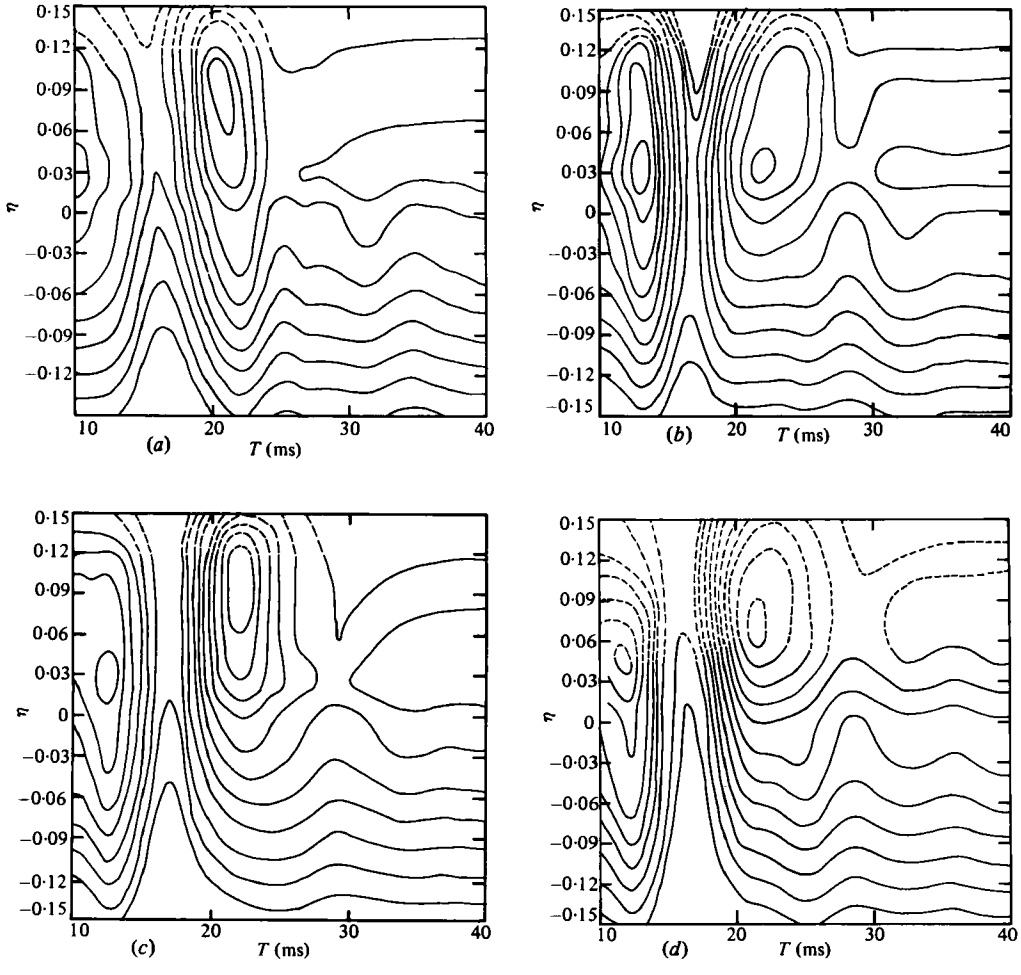

FIGURE 2. Contours of pseudo-stream-function $\langle\psi\rangle$ for $x/D = 1{\cdot}5$: (*a*) $\alpha = 45°$; (*b*) $\alpha = 90°$; (*c*) $\alpha = 135°$; (*d*) $\alpha = 180°$.

and 0° (see II) are similar, but the contours at $\alpha = 90°$ and 180 are somewhat different. These differences are small and can be attributed to the limited η locations at which data were taken and to the limited number of realizations used (forced by the extremely time-consuming data-analysis requirements). The dashed lines indicate extrapolated contours outside the region of actual data.

Note that the apparent structure in front (i.e. at lower T) of the spot, indicated by closed contours, in each $\langle\psi\rangle$ contour figure, is an artifact of the time-alignment procedure used in signal enhancedment (see II). The smaller structures following the spot (i.e. at larger T) are not the remnants of the boundary-layer spot (see later), but are results of data having been taken at a limited number of radial locations. The close agreement between the $\langle\psi\rangle$ contours presented in II and in this paper (figures 2*a*, 3*a*, 4*a*) is a clear demonstration that, for the $\langle\psi\rangle$ contours, u_p data at close η locations are not necessary.

Figure 5 shows the traces of phase-average longitudinal and lateral velocities $u_p(T)$, $v_p(T)$ for station 1. Cases (*a*), (*b*), (*c*) and (*d*) show data for $\alpha = 45°$, 90°, 135°

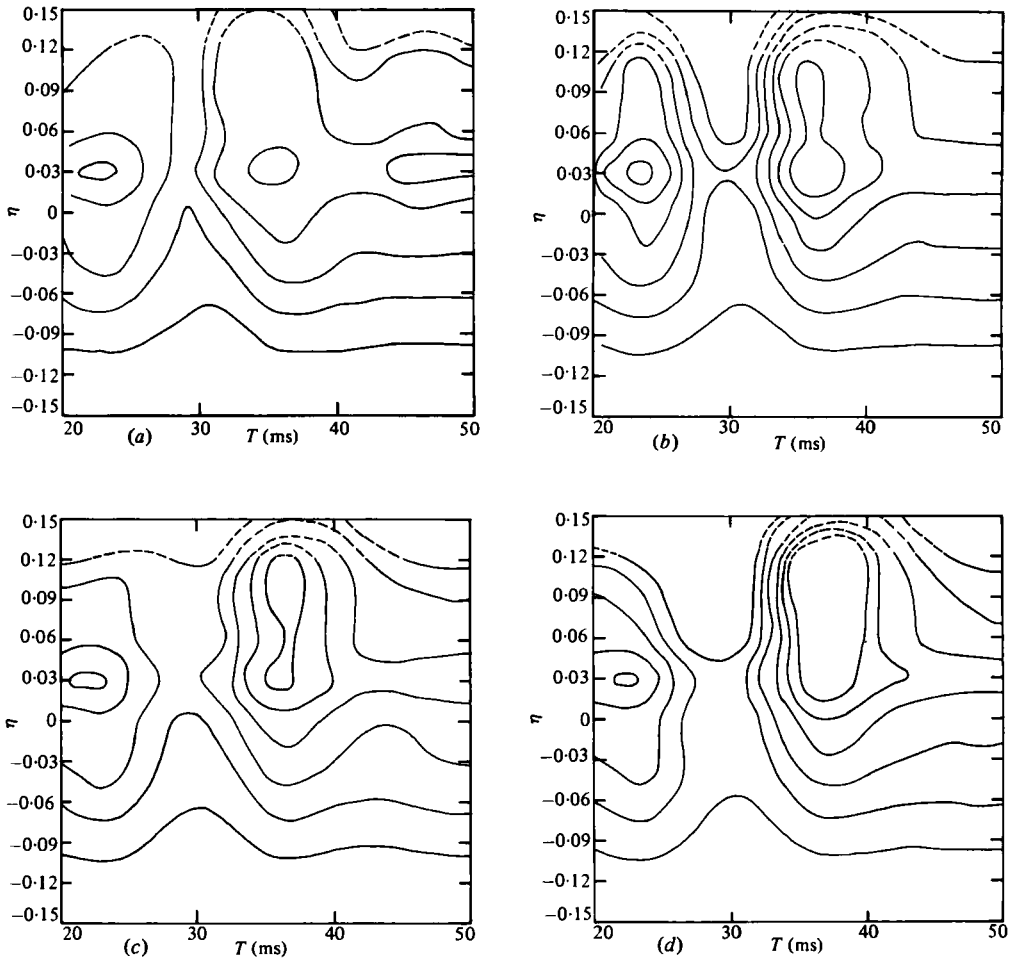

FIGURE 3. Contours of $\langle\psi\rangle$ for $x/D = 3{\cdot}0$: (*a*) $\alpha = 45°$; (*b*) $\alpha = 90°$; (*c*) $\alpha = 135°$; (*d*) $\alpha = 180°$.

and 180°, respectively. The scales for u_p/U_e and v_p/U_e shown as inserts in figure 5(*a*) are the same for figures 5(*b*), (*c*) and (*d*). It is impressive that data at different α agree quite well; for example, compare figures 5(*a*) and 5(*c*). The strong similarity of the $u_p(T)$, $v_p(T)$ traces suggests an axisymmetric structure at $x/D = 1{\cdot}5$. Since it is unlikely that a localized spot in the mixing layer can spread in the spanwise direction all around the mixing layer within the streamwise length $x/D = 1{\cdot}5$, it appears that the spark induces an essentially axisymmetric structure. This clearly points to the need for a study of the structure formation mechanism farther upstream. As will be demonstrated, the boundary-layer spot, although triggered by the spark, does not play an important role in the development of the shear-layer spot.

It is also impressive that the $\langle\psi\rangle$ contours, computed from the $u_p(T)$ data, suggest a spot structure consistent with the independent $v_p(T)$ data. In a frame convected with the structure, the fluid on the high-speed side of the shear layer moves downstream and that on the low-speed region moves upstream. Across the structure centre, say at $T \simeq 21{\cdot}5$ ms at $x/D = 1{\cdot}5$, jet core fluid is transported radially outward at the front of the spot and the ambient fluid transported inward at the

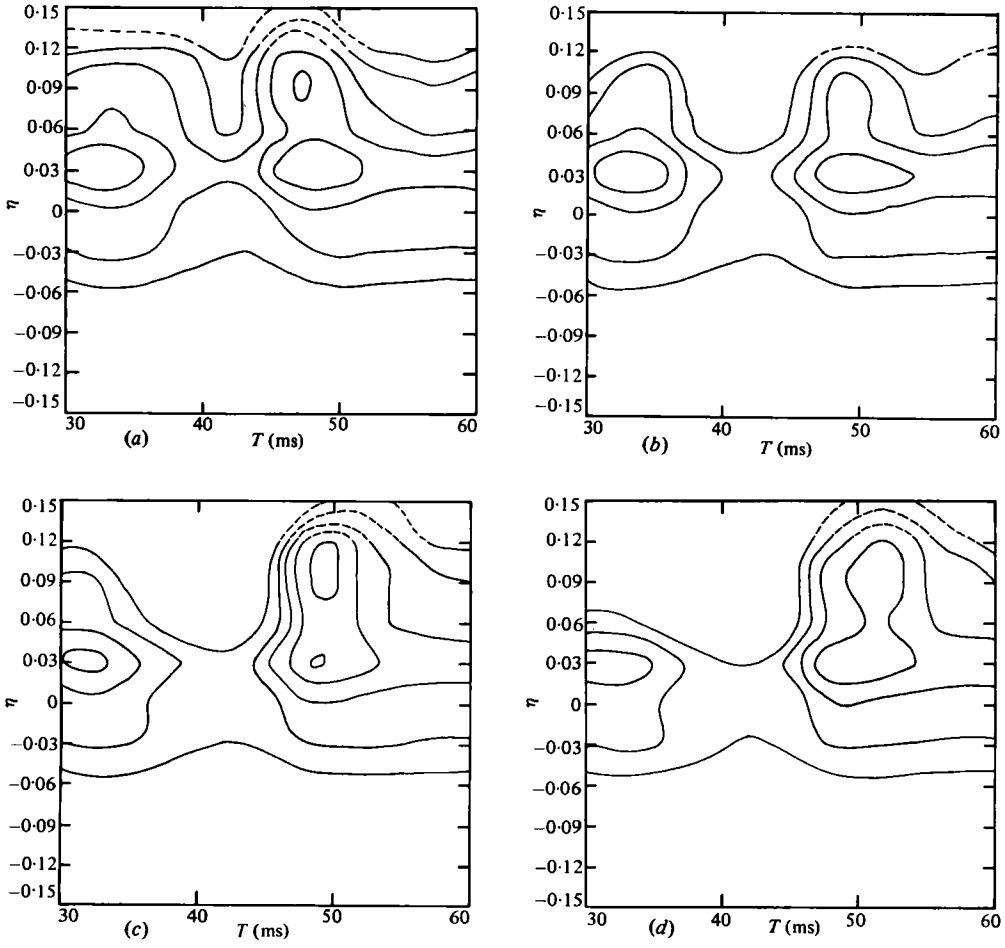

FIGURE 4. Contours of $\langle\psi\rangle$ for $x/D = 4{\cdot}5$: (*a*) $\alpha = 45°$; (*b*) $\alpha = 90°$; (*c*) $\alpha = 135°$; (*d*) $\alpha = 180°$.

back. So v_p must be positive for $T \leqslant 21{\cdot}5$ ms and negative for $T \geqslant 21{\cdot}5$ ms, as is indeed confirmed by the $v_p(T)$ data in figure 5(*a*). Note that, with respect to the spot centre, the rise of v_p to its peak value at lower T is sharper than the rise from the lowest peak at larger T. This suggests that the spot has a sharper front at the downstream end and a more diffuse back, a picture also suggested by the $\langle\psi\rangle$ contours. It is impressive that at an angle 180° away from the radius through the spark centre, the measurement technique can educe a strong 'footprint' as shown in figure 5(*d*).

For the sake of brevity, similar $u_p(T)$, $v_p(T)$ traces have not been shown for stations 2 and 3. However, the agreement between the peak values of the phase-average $u_p(T)$, $v_p(T)$ at different α is similar.

Figure 6 shows the traces of phase-average intermittency γ_p and coherent Reynolds stress $u_p v_p/U_e^2$ for $x/D = 1{\cdot}5$. Cases (*a*), (*b*), (*c*) and (*d*) represent $\alpha = 45°$, 90°, 135° and 180°, respectively. The scales for $u_p v_p/U_e^2$ and γ_p shown as inserts in figure 6(*a*) are the same for figures 6(*b*), (*c*) and (*d*). It is interesting to compare the γ_p peaks with the spot centres. The locations of peak γ_p (for example, in figures 6*a* and 6*b*) agree well with the centre of spots as denoted by corresponding $\langle\psi\rangle$ contours

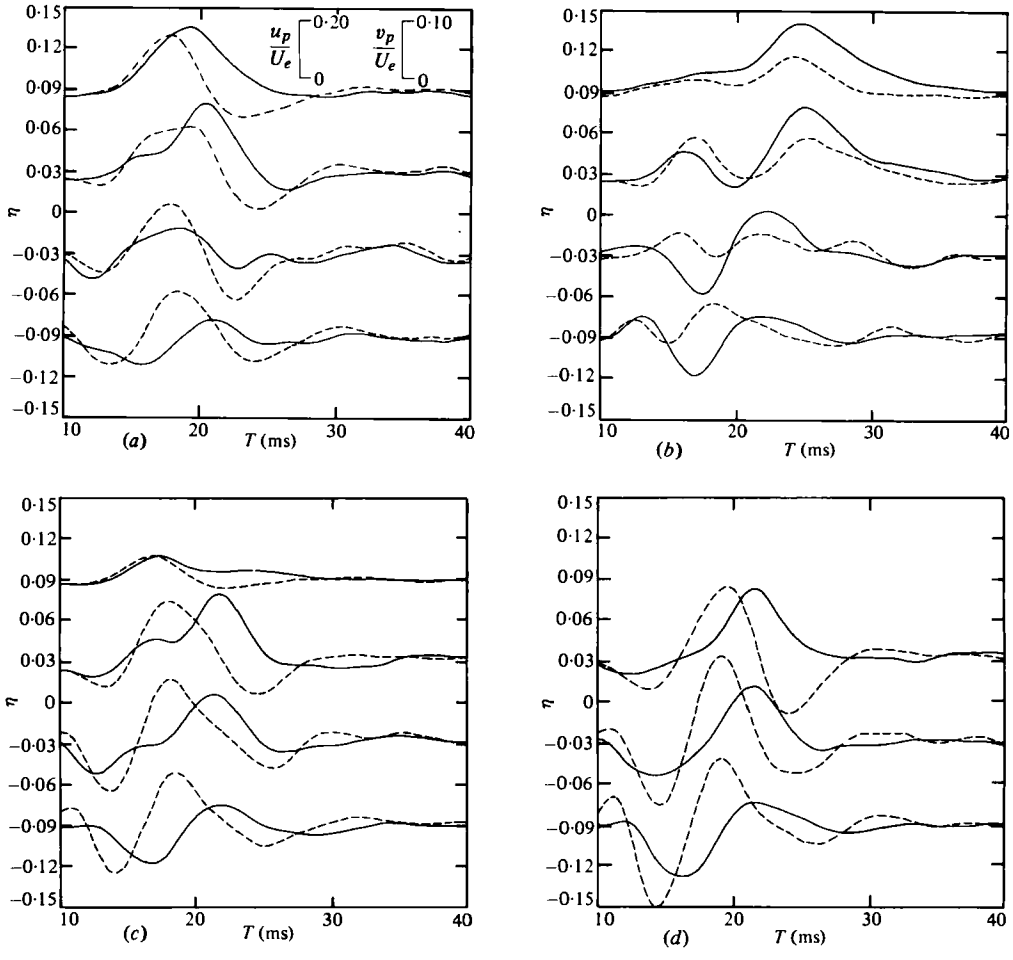

FIGURE 5. Traces of phase average u_p/U_e (solid line) and v_p/U_e (dotted line) for $x/D = 1{\cdot}5$: (a) $\alpha = 45°$; (b) $\alpha = 90°$; (c) $\alpha = 135°$; (d) $\alpha = 180°$.

(figures 2a, b). The spot transports jet core fluid outwards at its front. Thus, immediately in front of it on the high-speed side, the spot will be most often bounded by potential fluid and the phase average intermittency should be low, as indicated by the valleys in the γ_p traces, especially in figures 6(a), (c) and (d). Since the spot also entrains ambient potential fluid at its back, γ_p should also fall off from the spot-centre peak values on the outer edge, as shown in figures 6(a), (b) and (d). Note that $u_p v_p$ represents total coherent structure transport in the laboratory frame and includes terms like $U\tilde{v}_p + \tilde{u}_p V$. Thus, on the high-speed side, $u_p v_p$ will be dominated by the core fluid velocity U_e. The mean velocities being very low on the low-speed side, large $u_p v_p$ there represents the true turbulent transport by the spot. Thus, locations of $u_p v_p$ peaks on the low-speed side should agree with those of γ_p peaks (see for example, figures 6a, b).

The agreement between the locations of the spot centre based on γ_p contours and $\langle\psi\rangle$ is impressive. $\langle\psi\rangle$, being defined on the basis of the coherent-structure phase-average velocity u_p, is weighted by the low-frequency content of the signal, i.e. by

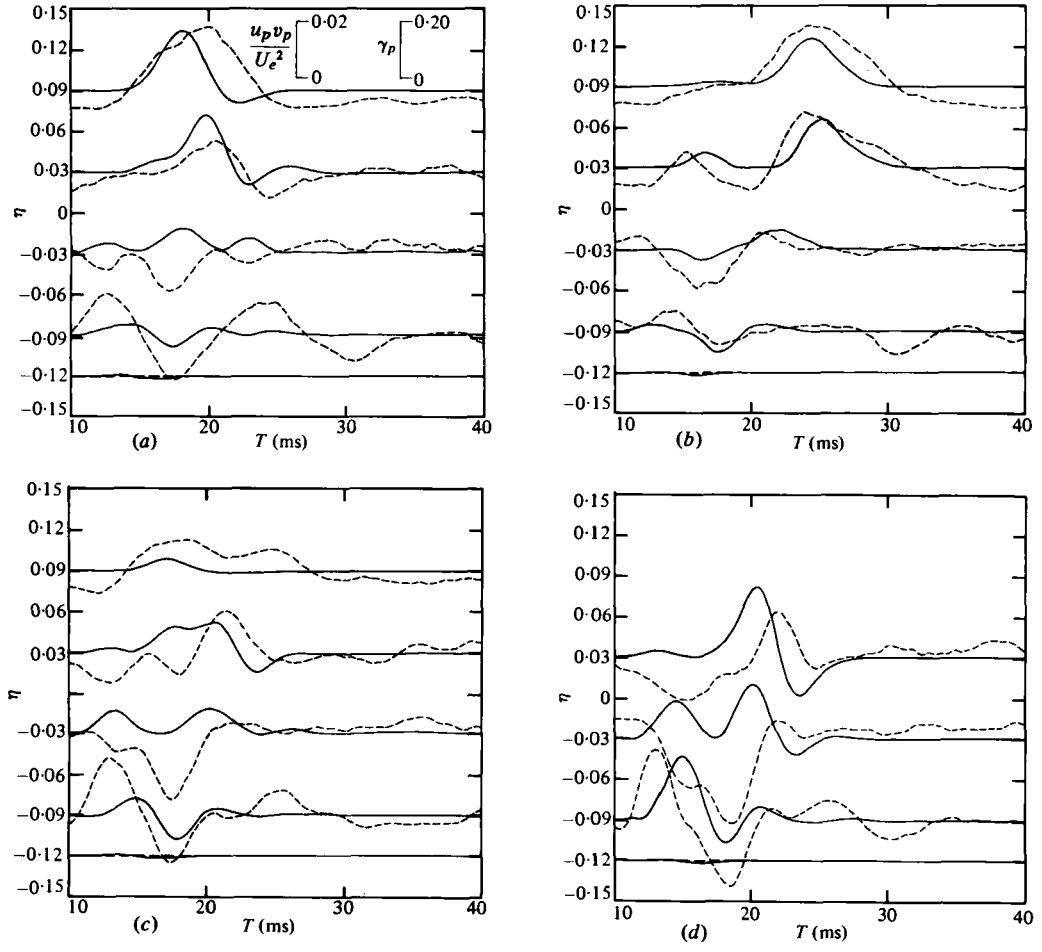

FIGURE 6. Traces of coherent Reynolds stress $u_p v_p / U_e^2$ (solid line) and phase average intermittency γ_p (dotted line) for $x/D = 1{\cdot}5$: (*a*) $\alpha = 45°$; (*b*) $\alpha = 90°$; (*c*) $\alpha = 135°$; (*d*) $\alpha = 180°$.

the underlying large-scale structures. γ_p on the other hand, is determined on the basis of the $\partial v/\partial t + A\partial v^2/\partial t^2$ signal (see II) and thus is weighted on the high-frequency, small-scale turbulence. The agreement of the spot centre determined by these two independent measurements provide further confidence in the signal eduction technique used and in the suggestion made earlier that $\langle \psi \rangle$ contours are particularly helpful in identifying the centres and boundaries of the relatively weak coherent structures and their convection velocities (see II; Hussain & Zaman 1980).

With respect to the spot centre, identified by $\langle \psi \rangle$ contours or peak values of γ_p, note that the peak value of $u_p v_p$ occurs at somewhat earlier time. That is, the front part of the spot produces much more Reynolds stress than the back part (for example, see figures 6*a*, *d*). This is to be expected since the front of the spot is marked by intense shear while the back is quite diffuse. It is also important to note that the positive peak in $u_p v_p$ at the front is significantly larger than the time mean value, which can be inferred from the $u_p v_p$ traces at larger T values. This time mean value, however, also includes UV and thus is much larger than the Reynolds stress $\overline{uv}$

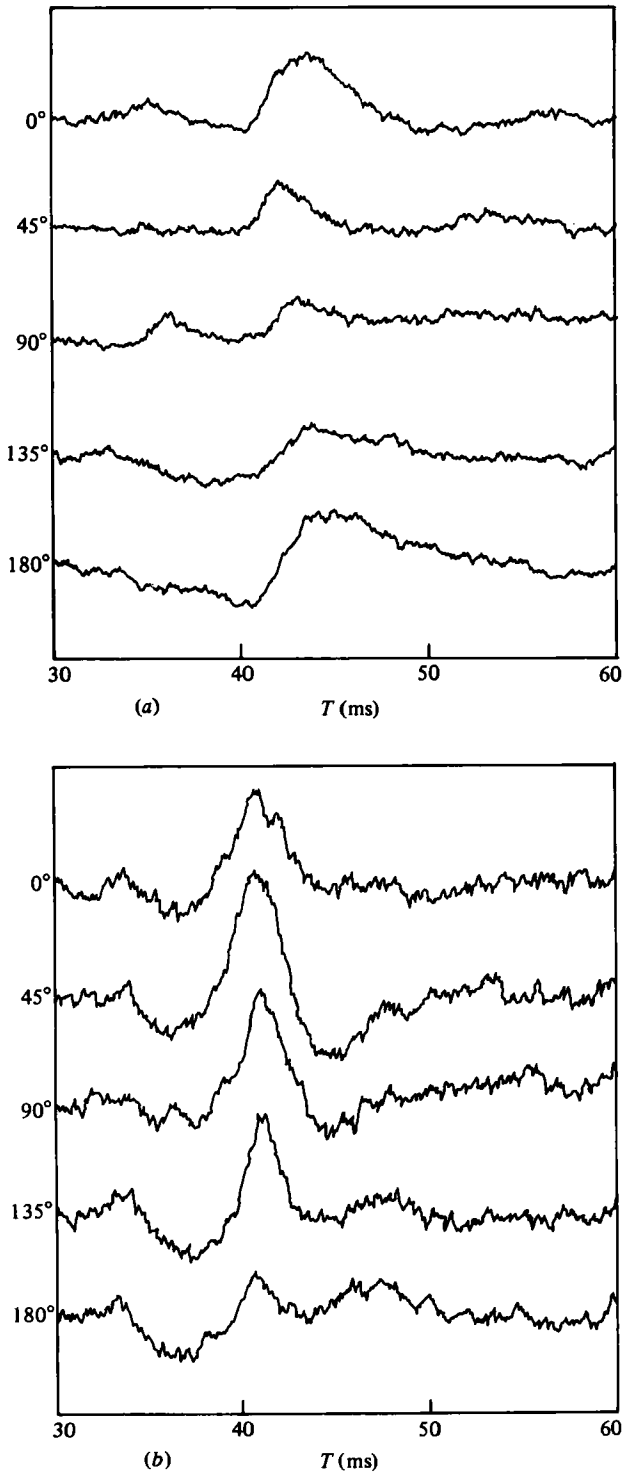

FIGURE 7. Phase-average velocity *without alignment* for $x/D = 4{\cdot}5$ at various angles: (*a*) u_p/U_e; (*b*) v_p/V_e.

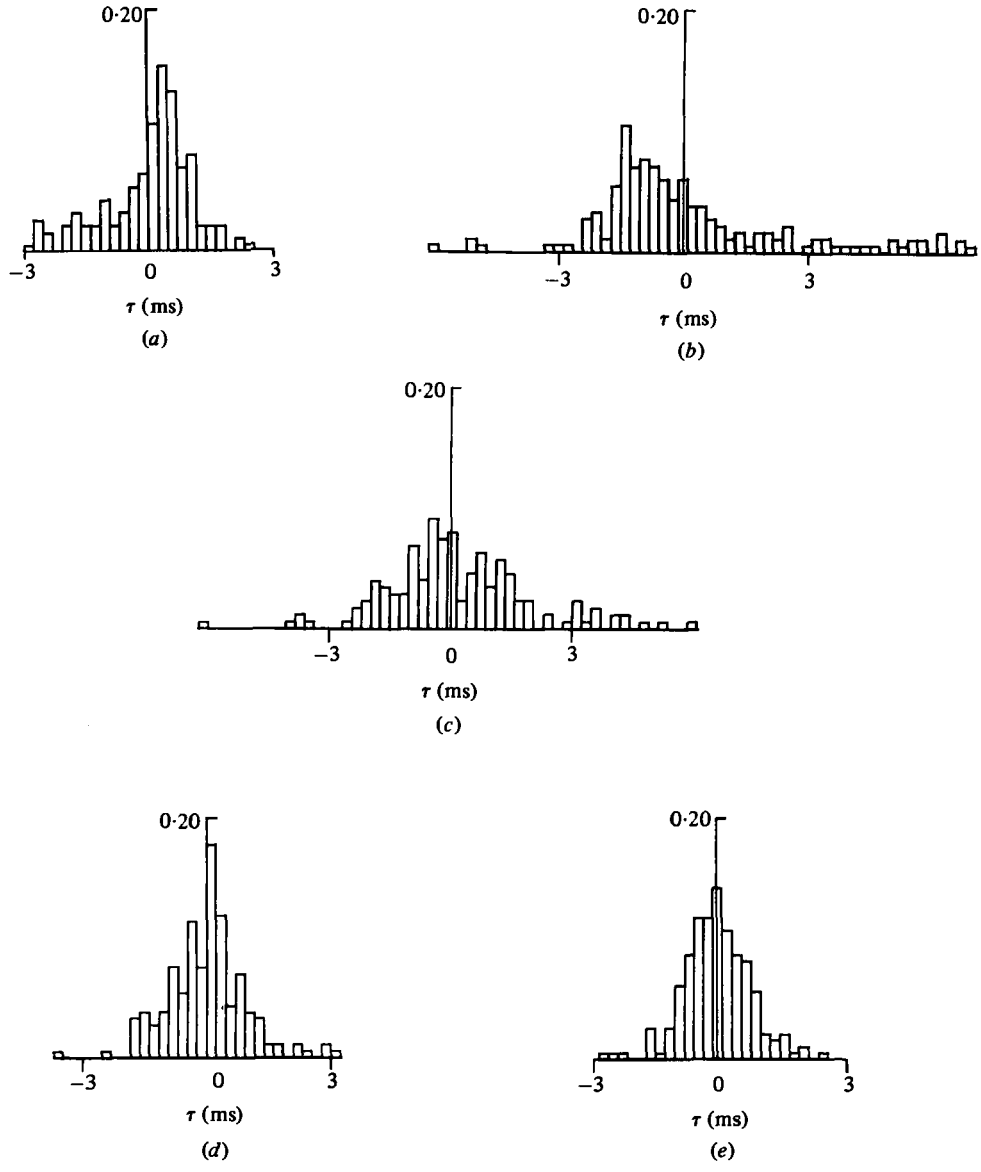

FIGURE 8. Histograms of time shifts for alignment at $x/D = 1{\cdot}5, \eta = 0$: (*a*) $\alpha = 0°$, (*b*) $\alpha = 45°$; (*c*) $\alpha = 90°$; (*d*) $\alpha = 135°$; (*e*) $\alpha = 180°$.

based on the classical Reynolds decomposition. Thus, significant Reynolds stress production is associated with the spot.

The traces of u_r', v_r', $\langle u_r v_r \rangle$ at different α planes look essentially similar to those at the $\alpha = 0°$ plane and are not presented. For the corresponding traces in the $\alpha = 0°$ plane, see II.

A concern of all signal-enhancement techniques is that the results may exhibit features resulting from the technique used. Figures 7(*a*, *b*) show the ensemble average u_p and v_p at $\eta = 0$ and $x/D = 4{\cdot}5$ for $\alpha = 0°$, 45°, 90°, 135° and 180° *without* alignment. These figures confirm that the axisymmetry of the average

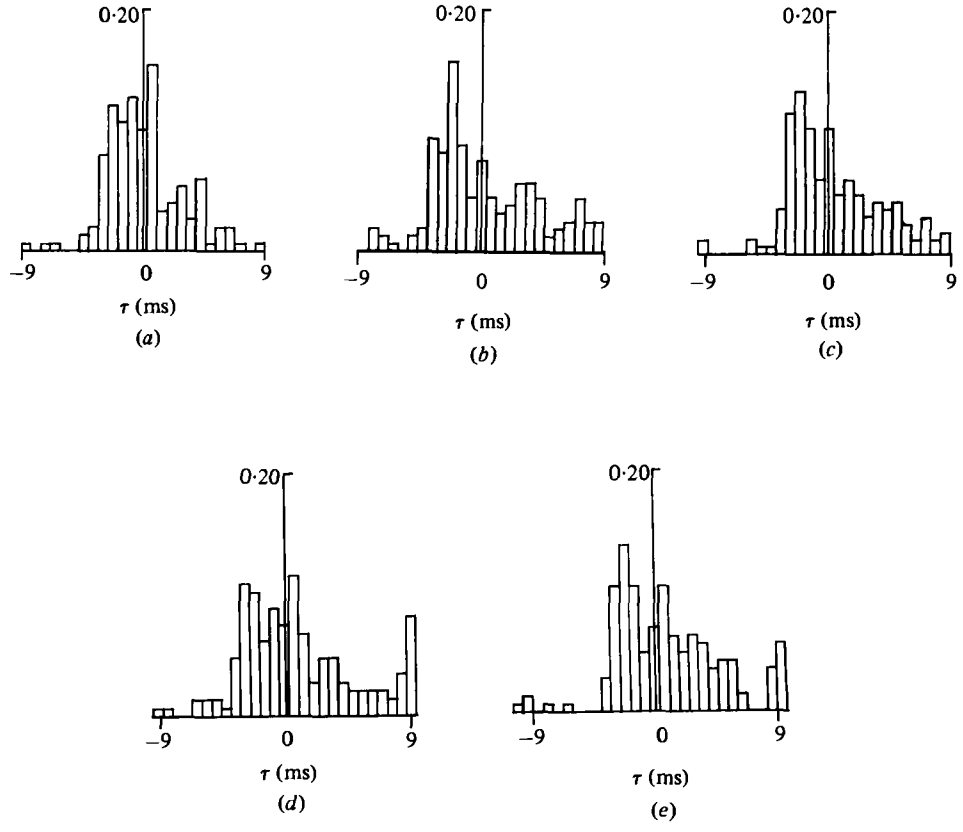

FIGURE 9. Histograms of time shifts for alignment at $x/D = 4{\cdot}5$, $\eta = 0$: (*a*) $\alpha = 0°$; (*b*) $\alpha = 45°$; (*c*) $\alpha = 90°$; (*d*) $\alpha = 135°$; (*e*) $\alpha = 180°$.

structure is not an artifact of the alignment procedure and rejection of 'freak' realizations; we can thus say that our eduction technique simply enhances the existing spot signatures. Note that the peak velocity in the unaligned traces is about 48 % for u_p and 97 % for v_p as compared with the corresponding aligned ensemble averages. This is a direct assessment of the effect of the alignment and rejection procedures which, rather than creating artificial structures, merely enhances the structure signature by eliminating the smearing effect inherent in ensemble-averaging of unaligned velocity signals.

Further information regarding the axisymmetry of the phase average structure is provided by the histograms of the time shifts required for the alignment process. Figures 8 and 9 show histograms for alignment at selected locations. The window width at $x/D = 1{\cdot}5$ in figure 8 is two sample times ($\sim 0{\cdot}24$ ms) and at $x/D = 4{\cdot}5$ in figure 9 it is six sample times ($\sim 0{\cdot}72$ ms). Thus, the figures have been scaled to compensate for a linear growth with x/D. The similarity of these histograms show both the axisymmetry at each x/D as well as a roughly linear increase in time shifts required for alignment as a function of x/D. It is also impressive that the standard deviation of the time shifts required for alignment is approximately $\sigma \sim 1{\cdot}5x/D$ compared with a structure passage time of about $15x/D$. Thus the rejection criterion of 3σ is still a fraction of the structure passage time. Note that the histograms are

presented for the $\eta = 0$ transverse location (that is, the middle of the mixing-layer width) which provides the severest test of axisymmetry.

3.2. *Spot formation mechanism*

The apparent axisymmetry of the structure for $x/D \lesssim 1{\cdot}5$ is not what one might expect from a localized intense disturbance as that produced by the spark near the lip of the shear layer. Sparks or other localized disturbances in a laminar boundary layer produce the boundary-layer spot which is also localized (Wygnanski *et al.* 1976; Cantwell *et al.* 1978). There is no reason to expect that a localized spot at the exit can spread spanwise fast enough to occupy the shear layer all around before the station 1, i.e. the streamwise location $x/D = 1{\cdot}5$. The axisymmetry of the phase-average signature of the spot initially appeared rather intriguing and in need of careful scrutiny. It was decided to explore the flow field between the lip and station 1 in order to explain the mechanism of formation of the spot and its interaction with the localized boundary-layer spot.

Data were taken in the near field ($0{\cdot}02 \leqslant x/D \leqslant 1{\cdot}5$) along the transverse line corresponding to $\eta = 0{\cdot}06$. In order to determine the azimuthal dependence of the data, these were taken in the two azimuthal planes corresponding to $\alpha = 0°$ and 180°. The streamwise evolutions of $u_p(T)$ traces are shown in figures 10(a, b) for $\alpha = 0°$ and $\alpha = 180°$, respectively. The corresponding $v_p(T)$ traces are shown in figures 11(a, b). Note that two traces representing phase averages based on two independent sets of measurements are included in figures 10(b) and 11(b) in order to indicate repeatability of the data. Note also that the traces at small x in figures 10(b) and 11(b) are shown for shorter time intervals.

Consider $u_p(T)$ traces for $\alpha = 0°$, i.e. for the plane bisecting the spark. Immediately downstream from the lip, there is only one structure (centred around $T = 5{\cdot}5$ ms). This is the boundary-layer spot. A second structure is detected farther downstream, i.e. at $x/D \simeq 0{\cdot}1$. As will be shown, this is a natural instability mode of the shear layer triggered acoustically by the spark. This structure grows rapidly, dominates the boundary-layer spot further downstream and becomes the spot discussed in this paper. The shear-layer spot progressively overshadows the boundary-layer spot and beyond $x/D \simeq 1$ the boundary-layer spot completely loses its identity. This is supported by the $v_p(T)$ traces also. Note that, for $x/D < 0{\cdot}5$, the two spots co-exist. The locus of an identifiable feature of the $u_p(t)$ signal or $v_p(t)$ signal in the (x, t) plane indicates the space–time trajectory of the spot, and thus the slope of this locus can be regarded as an indication of a convection velocity of the spot.

Considering the peak of u_p as an identifiable feature, the time of occurrence of this peak as a function of x is shown by the dotted line in figures 10(a, b) for $\alpha = 0°$ and 180°. Figure 10(a) shows that, downstream from the lip, the boundary-layer spot travels with a slightly higher convection velocity than the shear-layer spot. The two tend to merge, the merger being complete at $x/D \simeq 1{\cdot}0$. It is important to note that the boundary-layer spot shows little or no amplification due to the lack of a sustaining mechanism and appears to become diffuse starting at $x/D \simeq 0{\cdot}2$. The convection velocity appears to be about $0{\cdot}5U_e$ up to $x/D \simeq 0{\cdot}5$ but slightly larger further downstream. If convection velocity is determined from the points where u_p crosses zero value, from negative to positive with increasing time, a convection velocity of $0{\cdot}59U_e$ is obtained. Since this crossing point occurs near the middle of

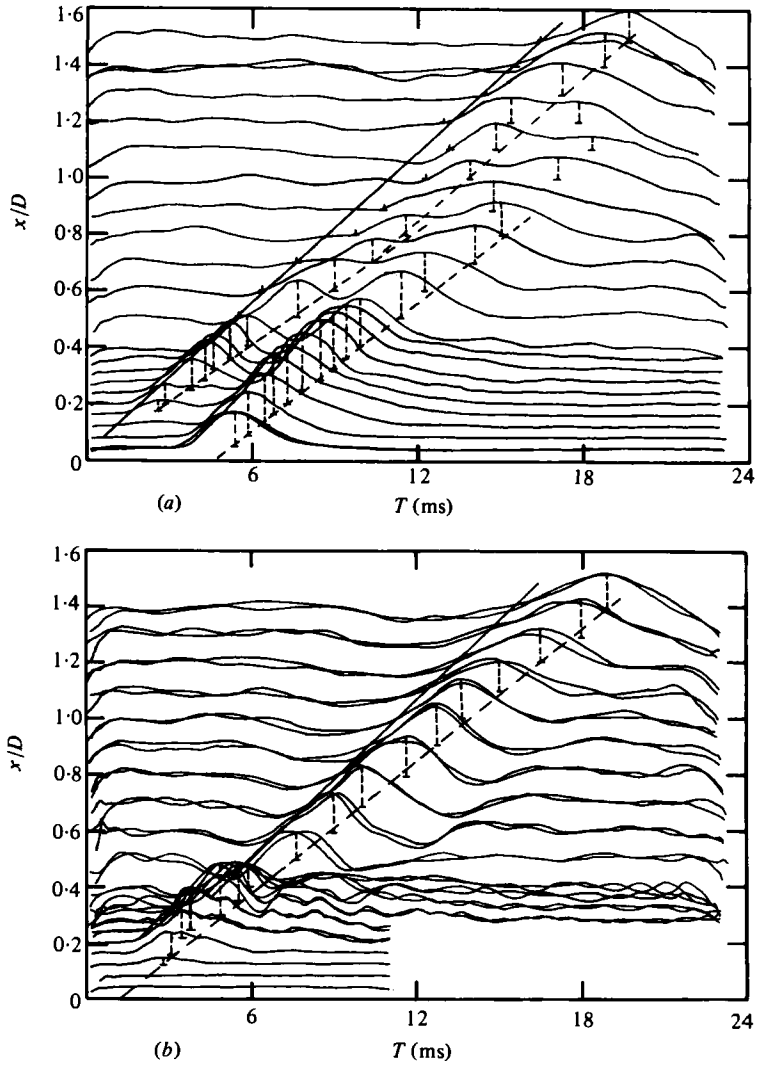

FIGURE 10. Streamwise evolutions of u_p/U_e traces along the line $\eta = 0{\cdot}06$; (*a*) $\alpha = 0°$; (*b*) $\alpha = 180°$.

the spot, this value should be more representative of the overall convection velocity of the spot. Similar convection velocities result from the $u_p(T)$ traces at $\alpha = 180°$.

If the $v_p(T)$ traces are considered, the space–time trajectory of the same feature, i.e. the zero crossing point, produces a convection velocity of $0{\cdot}61U_e$.

Note that these convection velocities agree with the value $0{\cdot}6U_e$ found by Hussain & Clark (1981) from high-speed flow-visualization ciné film in the axisymmetric mixing layer. Furthermore, even though convection velocities inferred from figures 10 and 11 are significantly lower than the value of $0{\cdot}72U_e$ measured by Yule (1978), these results are in essential agreement with the data of Ko & Davies (1971), Lau, Fisher & Fuchs (1972), Bradshaw, Ferriss & Johnson (1964) and Petersen (1978). For an explanation of the differences among convection velocities measured by different investigators, see Hussain & Zaman (1981). Of course, in the situation where two coherent structures undergo interactions like pairing, the convection

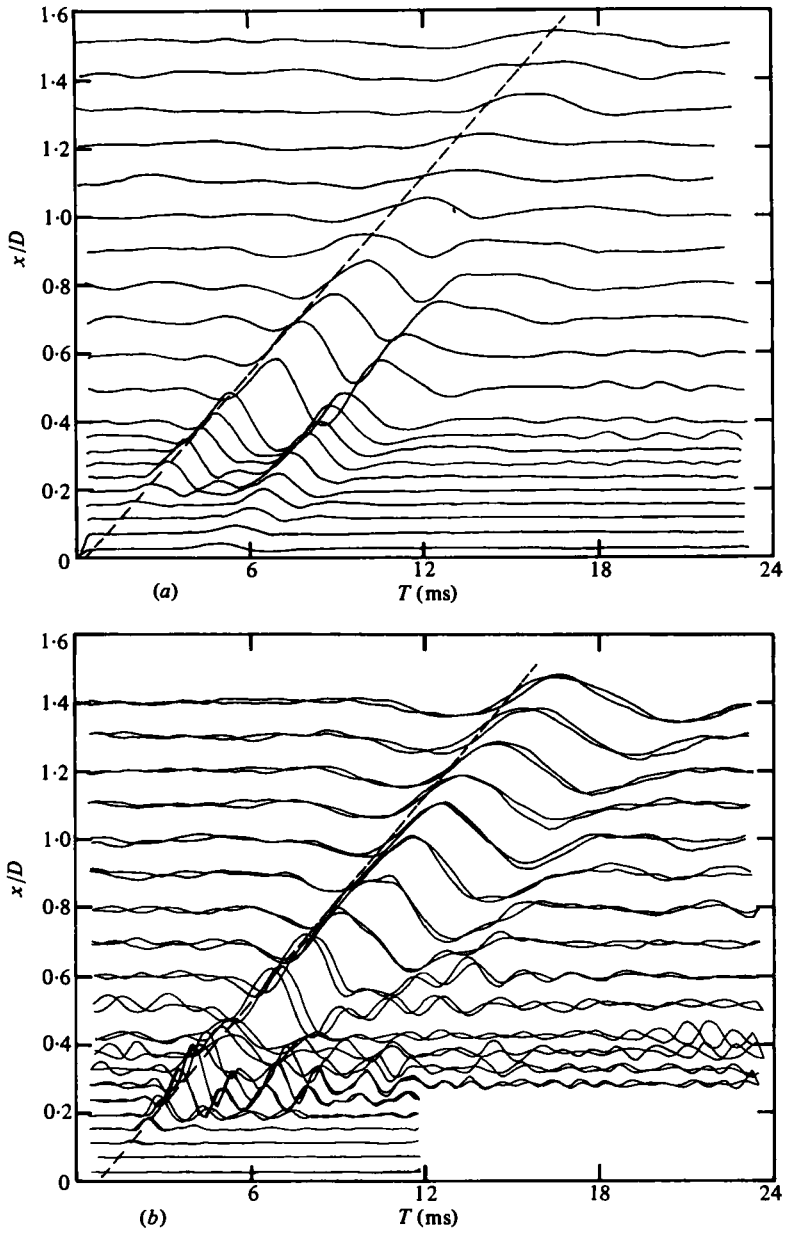

FIGURE 11. Streamwise evolutions of v_p/U_e along the line $\eta = 0{\cdot}06$: (*a*) $\alpha = 0°$; (*b*) $\alpha = 180°$.

velocity can vary widely (Browand & Laufer 1975; Bruun 1977; Zaman & Hussain 1980). It is important to note that the inferred convection velocity will depend upon the type or feature of the signal used. For example, the convection velocity of the front or the back of the spot is not that of the spot centre, owing to progressive increase with x of the spot size. As demonstrated in II, neither u_p nor v_p nor vorticity contours identify the boundary of the spot. Thus, the convection velocity based on the spot front as indicated by the v_p traces is not expected to be the same as that based on the u_p traces since the fronts indicated by these two traces are not identical.

Furthermore, the relative difference is a function of the radial location in the free shear layer (see figures 5*a–d*).

It is interesting to note that, in the absence of the boundary-layer spot (i.e. $\alpha = 180°$), the velocity signal is essentially periodic, indicating the natural instability of the free shear layer. The $v_p(T)$ signal at $x/D \simeq 0{\cdot}3$ shows it more clearly than the $u_p(T)$ signal. This periodicity does not appear in the azimuthal plane of the spark, i.e. $\alpha = 0°$, presumably because the signals there will align with the much stronger boundary-layer spot rather than the shear-layer instability mode which occurs randomly. At 180°, because of the absence of the boundary-layer-spot footprint, the signals align with the shear-layer instability mode itself and thus enhances the periodic footprint of the instability wave.

Note that the signal periodicity doubles on the average between $x/D = 0{\cdot}2$ and $x/D \simeq 0{\cdot}4$, suggesting one stage of pairing between the natural structures between these two stations. Considering the signal at $x/D \simeq 0{\cdot}2$, the frequency of the signal is about 1 kHz. The initial momentum thickness being about 0·0295 cm (see I), the corresponding momentum thickness Strouhal number of the initial shear layer is about 0·014. Studies of natural instability and roll-up in a number of shear layers in our laboratory (Husain & Hussain 1979*b*) have shown that the roll-up Strouhal number is about 0·013 and that the first pairing occurs at a distance of $x/\theta_e \simeq 150$ from the lip. Since $x/D = 0{\cdot}3$ corresponds to $x/\theta_e \simeq 130$, it would thus appear that the present results agree well with the previous study.

It is interesting to note in figures 10 and 11 that the highly periodic signal near the lip occurs upstream of the spot (i.e. at larger T) and not downstream. This suggests that the natural instabilities occur at random phase with respect to the spot before the spot passage but occurs at regular and repeatable intervals following the spot passage. That is, the spot somehow orders the instability mechanism for a while. This is particularly important because there can be preferential interaction between the spot and the naturally occurring structures at later times as compared with the spot and natural structures preceding the spot.

3.3. *Azimuthal dependence of the shear-layer instability*

Although the contours of the phase-average flow properties in different azimuthal planes show that the spark-induced coherent structure is axisymmetric 'on the (phase) average', the question whether each structure is individually axisymmetric needs to be answered. Clearly, such a question must be answered on the basis of instantaneous signals. To this end it was decided to monitor the velocity oscillations in the shear layer simultaneously by a number of sensors placed at different azimuthal points. A special fixture was designed to hold seven hot wires at equally spaced azimuthal locations and an eighth wire on the jet axis. All the probes were arranged such that the hot wires were aligned azimuthally in the same axial plane. At each x-location, the probes were shifted radially such that these were always at the radial location corresponding to $U/U_e = 0{\cdot}8$.

Figures 12(*a–d*) show the streamwise evolutions of the shear-layer instability by recording the time traces of the hot wires at successive x-locations. The top trace is that of the wire in the $\alpha = 0°$ plane (i.e. the plane bisecting the spark). The bottom trace in each figure is that of the hot wire on the jet axis and it has a negative

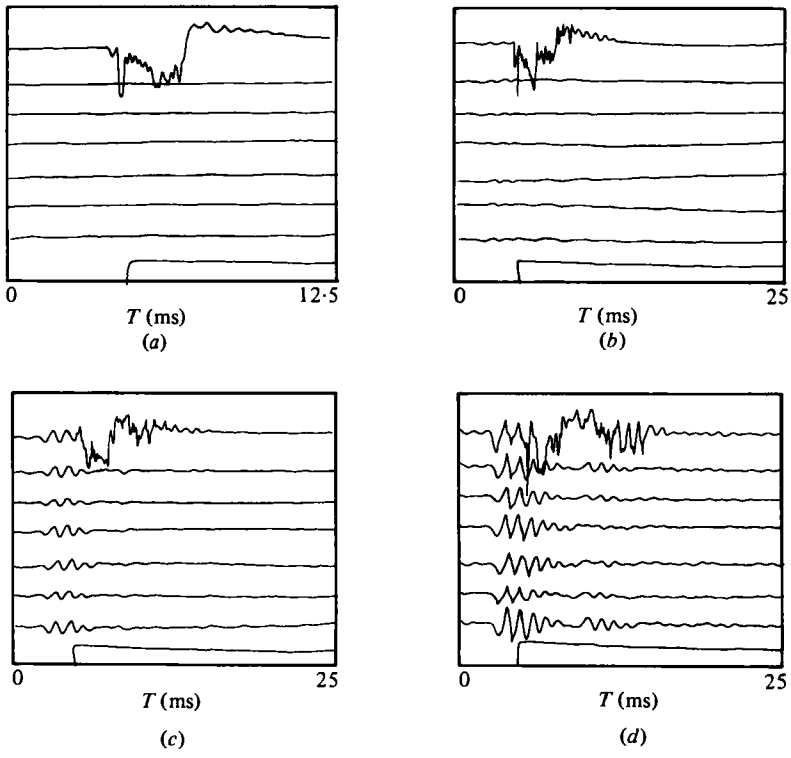

FIGURE 12. Azimuthal variation of initial instability. Top seven traces are from probes located at equidistant azimuthal locations at the radial location where $U/U_e = 0{\cdot}8$. The top trace is for $\alpha = 0°$. The bottom trace is from the eighth probe located on the jet centre-line. (*a*) $x/D = 0{\cdot}04$; (*b*) $x/D = 0{\cdot}08$; (*c*) $x/D = 0{\cdot}12$; (*d*) $x/D = 0{\cdot}16$.

pulse of duration 4·5 ms superimposed on it in order to provide time reference with respect to the firing of the spark. The top trace depicts the legacy of the boundary-layer spot in the shear layer. Note that, with increasing x, the boundary-layer spot footprint decreases in strength and is detected only by the wire directly in the path of the localized spot. Starting from $x/D \simeq 0{\cdot}08$ in the shear layer downstream (i.e. in front) of the spot, there is a shear-layer instability which grows rapidly in amplitude with x and which appears perfectly axisymmetric. Note that, at $x/D \gtrsim 0{\cdot}16$, the spot signature is stronger than the boundary-layer spot and the traces also show the initial stage of the natural instability of the free shear layer.

The spark-induced and natural instabilities of the shear layer are compared in figures 13(*a–d*). Figures 13(*a*, *b*) show the individual $u(t)$ traces with and without the spark firing. These two figures show that the velocity undulations in the spot are of the same frequency as those outside the spot and that the spot footprint is of larger amplitude. The shear-layer instability outside the spot is unaffected by the spot. Figure 13(*d*) shows another realization of the signals at the same location (i.e. $x/D \simeq 0{\cdot}2$) as in 13(*a*), but with an expanded time scale. Note that the front of the spot (i.e. the lower-T end) is exactly aligned azimuthally. It is impressive that the individual traces also agree in detail with each other over the range of the spot. Figure 13(*c*) shows the traces from the eight hot wires on a compressed time scale.

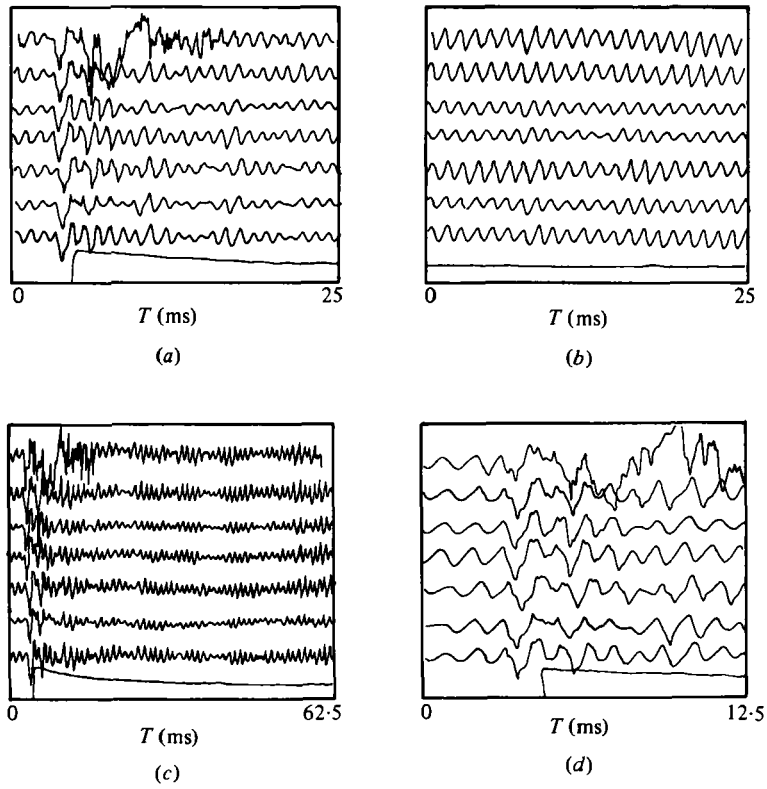

FIGURE 13. Azimuthal dependence of $u(t)$ traces at $x/D = 0{\cdot}20$. The top trace is for $\alpha = 0°$: (*a*) with spark; (*b*) without spark; traces in (*c*) and (*d*) correspond to excited cases in compressed and expanded time scales.

It is interesting to note that, sufficiently far away from the spot signature, the natural instability signatures are amplitude modulated. Even though the amplitude modulation is random in duration, the modulation appears essentially axisymmetric. This clearly suggests that the natural instability mode in the jet is also axisymmetric. The variations between amplitudes of the signal traces may not necessarily reflect inherent azimuthal variation in amplitude. These variations may be due to very slight variation in the radial positioning of the wires in the axisymmetric mixing layer.

Figures 14(*a–d*) show the differences between the shear-layer instabilities with and without the spark at $x/D = 0{\cdot}24$ and $0{\cdot}28$. It is clear that the spot-velocity field is not dominant over the natural structures starting with $x/D \simeq 0{\cdot}28$ as it is at smaller x. The strong tendency to form a subharmonic is indicative of initiation of vortex pairing. Associated with the pairing is also an indication of breakdown starting at $x/D = 0{\cdot}28$. Comparing the signals outside the spot with the signals in the absence of the spot, it is clear that the spot has no influence on the natural instability of the shear layer between the spots. Note that, since the spot duration is about 4 % of the time between successive sparks, two successive spots do not interact with each other even though these might interact with the naturally occurring ones.

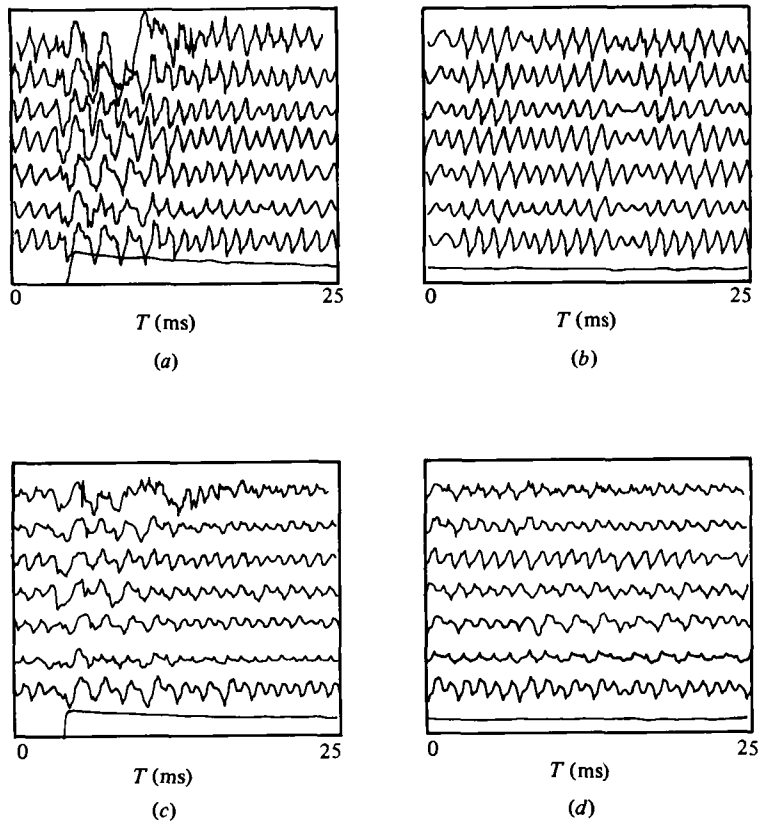

FIGURE 14. Azimuthal dependence of $u(t)$ traces: (*a*) with spark at $x/D = 0{\cdot}24$; (*b*) without spark at $x/D = 0{\cdot}24$; (*c*) with spark at $x/D = 0{\cdot}28$; (*d*) without spark at $x/D = 0{\cdot}28$.

4. Concluding remarks

There is excellent agreement between the contours of phase-average measures of the coherent motions in the free shear-layer spot in different azimuthal planes. The spark induces both a boundary-layer spot and a shear-layer instability mode. The latter is excited in the free shear layer at the location of its maximum susceptibility by the acoustic disturbance of the spark, presumably in a manner not unlike the creation of naturally occurring large-scale structures. (It has been found that, in the absence of the spark, hand clapping near the shear layer can induce similar instability modes of the shear layer.) The boundary-layer spot slows down as it enters the free shear layer and convects downstream while trailing the shear-layer spot. The rapid growth of the shear-layer spot overshadows the boundary-layer spot at $x \simeq 0{\cdot}5$, the latter disappearing by $x/D \simeq 1{\cdot}0$ through decay and interaction with the shear-layer spot.

Natural instability of the initially laminar axisymmetric mixing layer has been shown in many early investigations to be axisymmetric, even though all such studies involved small jets. It is impressive that the natural instability is axisymmetric even in a large jet and especially when the instability wavelength is considerably smaller than the jet diameter. The spot footprint in the mixing layer is essentially

axisymmetric. The natural instability in the shear layer is amplitude modulated in a random manner. Both the instability and the modulation are also axisymmetric. Thus, the spark-induced spot is axisymmetric not only on the phase-average basis but also individually.

From the footprints of the spot at different x stations, the spot convection velocity can be inferred. However the convection velocity computed as such will be noticeably dependent on the signal feature chosen. For example, because of the fairly rapid increase with x of the spot size (i.e. streamwise length), the locus of the peak of $u_p(t)$ signal will give a lower velocity that the front would. It is shown that the spot travels at about $0{\cdot}6U_e$, which agrees with earlier study based on high-speed visualization pictures of coherent structure motion in an axisymmetric free shear layer.

The research was supported by the National Science Foundation under grant ENG-7822110 and the Office of Naval Research under grant N00014-76-C-0128.

REFERENCES

Bradshaw, P. 1977 *J. Fluid Mech.* **80**, 795.

Bradshaw, P., Ferriss, D. H. & Johnson, R. F. 1964 *J. Fluid Mech.* **19**, 591.

Browland, F. K. & Laufer, J. 1975 *Turbulence in Liquids* **4**, 333. University of Missouri - Rolla.

Bruun, H. H. 1977 *J. Fluid Mech.* **83**, 641.

Cantwell, B. J. Coles, D. & Dimotakis, P. 1978 *J. Fluid Mech.* **87**, 641.

Husain, Z. D. & Hussain, A. K. M. F. 1979*a* *A.I.A.A. J.* **17**, 48.

Husain, Z. D. & Hussain, A. K. M. F. 1979*b* *Bull. Am. Phys. Soc.* II **24**, 1144.

Hussain, A. K. M. F. & Clark, A. R. 1981 *J. Fluid Mech.* **104**, 263.

Hussain, A. K. M. F., Kleis, S. J. & Sokolov, M. 1980 *J. Fluid Mech.* **98**, 97.

Hussain, A. K. M. F. & Zaman, K. B. M. Q. 1980 *J. Fluid Mech.* **101**, 493.

Hussain, A. K. M. F. & Zaman, K. B. M. Q. 1981 *J. Fluid Mech.* **110**, 39.

Ko, N. W. M. & Davies, P. O. A. L. 1971 *J. Fluid Mech.* **50**, 49.

Kotsovinos, N. E. 1976 *J. Fluid Mech.* **77**, 305.

Lau, J. C., Fisher, M. J. & Fuchs, H. V. 1972 *J. Sound Vib.* **22**, 379.

Petersen, R. A. 1978 *J. Fluid Mech.* **89**, 469.

Sokolov, M., Hussain, A. K. M. F., Kleis, S. J. & Husain, Z. D. 1980 *J. Fluid Mech.* **98**, 65.

Wygnanski, I., Sokolov, M. & Friedman, D. 1976 *J. Fluid Mech.* **78**, 785.

Yule, A. J. 1978 *J. Fluid Mech.* **89**, 413.

Zaman, K. B. M. Q. & Hussain, A. K. M. F. 1980 *J. Fluid Mech.* **101**, 449.

Zaman, K. B. M. Q. & Hussain, A. K. M. F. 1981 *J. Fluid Mech.* (to appear).

Zilberman, M., Wygnanski, I. & Kaplan, R. E. 1977 *Phys. Fluids Suppl.* **20**, 258.